Microscale modeling of nondilute flow and transport in porous medium systems

Timothy M. Weigand and Cass T. Miller[*]

Department of Environmental Sciences and Engineering, University of North Carolina, Chapel Hill, North Carolina 27599, USA

Nondilute transport occurs routinely in porous medium systems. Experimental observations have revealed effects that seemingly depend upon density, viscosity, velocity, and chemical activity. Macroscale models based upon averaged behavior over many pores have been relied upon to describe such systems to date, which require parametrization of important physical phenomena in material coefficients. To advance fundamental understanding of these complex systems, we examine nondilute transport from a fundamental microscale, or pore-scale, continuum modeling perspective. We approximate the solution of a model based upon the variable-density Navier-Stokes equations and a nondilute species transport equation. Known dependencies of the densities, viscosities, chemical activity, and diffusion for a salt solution on chemical composition are included in the model. Microscale model solutions are averaged to the macroscale and compared with extant experimental observations. Investigation of the effects of various physical phenomena on the microscale velocity distribution and the observed macroscale dispersion are considered using dimensional analysis and constrained simulations. Simulation results are used to explain observed experimental results in light of underlying mechanisms. Conditions under which the various physicochemical effects investigated are important are revealed.

I. INTRODUCTION

Nondilute solutions occur in a variety of porous medium physics applications, such as salt water intrusion, leachate transport, and density-motivated remediation [1–3]. Species transport in such systems differs markedly from common dilute systems. Macroscale mathematical models are used to represent the behavior of such systems in an averaged sense over a representative regions of the porous structure.

Laboratory experiments for nondilute flow and transport in porous media are complicated and time consuming. Experimental work has consisted of column experiments where various fluids and salts are used to adjust density, viscosity, chemical activity, fluid velocities, and pore morphology and topology characteristics [4–7]. While these experiments provide insight related to observed displacement patterns and solute profiles, it is difficult to extract a mechanistic understanding from the results due to the scale of the experiments and the complex and competing physical phenomena that are operative in such systems. An additional downside to such experimental work is the inability to isolate different physical phenomena, since such systems are constrained by the properties of the solutions investigated.

Attempts to model gravitationally stable, nondilute flow and transport in porous media have represented limited sets of laboratory data [6,7]. However, these models are dependent on fitting parameters that are not firmly tied to underlying physical phenomena that impact the transport phenomena observed [7,8]. Because our mechanistic understanding is lacking, extant modeling approaches are not predictive.

The use of highly resolved microscale, or pore-scale, computational simulations is one approach at overcoming the drawbacks of traditional laboratory experiments and obtaining mechanistic insight [9]. Microscale modeling can be used to simulate complex systems at a scale at which continuum mechanical models can be formulated rigorously and consistently with well-understood physics. The results from such simulations can in turn be used to gain fundamental insight needed to advance, evaluate, and validate macroscale models that are needed for the size of typical applications of concern. Additionally, microscale computational approaches enable a fuller exploration of potential physical phenomena because individual model parameters can be isolated and controlled. Despite the apparent benefits of microscale modeling to advance understanding of nondilute species transport in porous medium systems, such approaches have not been reported in the literature. A fundamental understanding of nondilute flow and transport in porous media at all spatial scales is lacking, and the predictive capabilities of macroscale models for nondilute transport are limited as a result.

II. OBJECTIVES

The goal of this to work is to advance mechanistic understanding of nondilute flow and transport in porous medium systems. The specific objectives are: (1) to formulate and approximate a microscale nondilute flow and transport model for porous media; (2) to examine microscale simulation results qualitatively and quantitatively to aid mechanistic understanding; (3) to upscale microscale simulation results and compare to extant experimental observations; and (4) to describe the effect of a set of physical phenomena on observed macroscale solute dispersion.

[*]casey_miller@unc.edu

III. BACKGROUND

The spatial scale of a mechanistic model is one of its defining features and determines the phenomena that need to be considered [9]. For a porous medium system, the microscale (also known as the pore scale) is where the boundaries of all phases and interfaces are known in both space and time. The macroscale is defined as the scale at which a point is represented by an average over a region of the system that contains all phases present. The minimum size of such an averaging region, such that averaged quantities are insensitive with respect to changes in the size of the region, is termed a representative elementary volume (REV) [10]. At the macroscale, variables such as porosity and volume fraction exist, both of which are ill-defined at the microscale. As a macroscale point is an average of the microscale behavior, the distribution of the underlying variable is lost. Due to the loss of information, underlying microscale transport phenomena may need to be parameterized in larger scale models. An example of this is the inclusion of mechanical dispersion in macroscale species transport models to account for the varied movement of the species due to the microscale fluid phase velocity distribution [10].

Dilute microscale and macroscale fluid flow and species transport in porous media has been studied extensively and the use of microscale computational simulations is commonplace [11–17]. Microscale simulations are frequently used to evaluate existing macroscale relationships for species transport [11,13], to investigate non-Fickian transport for various types of porous media [14,16], or to improve understanding of subscale effects on observed macroscale behavior [18]. Microscale simulations are preferred over laboratory experiments because the microscale flow field can be analyzed to better understand macroscale behavior. For example, the work of Aramideh *et al.* [14] found flow conditions needed for the existence of recirculation zones for media comprised of overlapping spheres. These zones resulted in regions of negative velocities relative to the mean direction of flow and explained the observed non-Fickian behavior. Much of the research for microscale dilute flow and transport has focused on examining microscale velocity distributions and correlations to describe macroscale behavior [14,16,19].

As compared to dilute flow and transport, microscale nondilute flow and transport studies have been limited to the membrane literature [20,21]. Gruber *et al.* [21] implemented a microscale model to assess impacts of concentration polarization on reverse osmosis and forward osmosis performance. The slightly compressible version of the Navier-Stokes equation were used to solve for the velocity field and the microscale transport equation was used to model the salt species. The impacts of nondilute behavior, including the resulting velocity field distribution, were not discussed or analyzed.

The thermodynamically constrained averaging theory (TCAT) is a continuum mechanical approach for deriving mechanistic macroscale models by directly averaging microscale conservation and thermodynamic equations and closing the macroscale models using an entropy inequality [9,22]. All variables, conservation equations, and thermodynamic laws are first written at the microscale and formal averaging approaches are used to derive the macroscale equations and variables. A constrained entropy inequality is formulated and used to guide model closure and ensure the resulting model obeys the second law of thermodynamics. TCAT models for single phase flow and transport in porous media [23,24], nondilute flow and transport in porous media [6,22] and two phase flow and transport in porous media have been developed [25,26]. The TCAT approach also uses specific notation to discern between scales and types of averages. For this work, we follow the TCAT notation and note only that variables adorned with subscripts are microscale variables and macroscale variables are adorned with superscripts.

With the TCAT approach, variables across all possible scales are consistent, well-defined, and connected. Due to this, microscale simulations can be performed and the results may be averaged to examine larger scale variables and phenomena. This is known as subscale modeling and is an approach to validate models where experiments at the scale of the model are not required. The benefit of this approach is that the physics at the microscale are typically well-defined and understood and variables that can be difficult to analyze and isolate experimentally are more easily quantified. This approach has seen success in other application including two-fluid-phase flow in porous media [27–30].

The most successful attempts at modeling macroscale nondilute flow and transport have extended Fick's law such that dispersion is a function of the composition [6–8,22,31–33]. Hassanizadeh [31] first developed the nonlinear Fickian model, which is a Taylor expansion of Fick's law and includes a fitting parameter to account for nondilute behavior. Weigand *et al.* [6] expanded on the nonlinear Fickian model by including activity impacts as well as an additional fitting parameter. This model was formulated with TCAT and outperformed the nonlinear Fickian model for the one dataset considered. However, the major drawback with these models is the lack of understanding of the mechanistic factors affecting the fitting parameters. The parameter in the nonlinear Fickian model has an exponential relation to the Darcy velocity but no fundamental mechanistic basis has been advanced to support the empirical form [7,8,34]. Applying the TCAT model to the same dataset used by Watson *et al.* [7] found a similar relationship where the fitting parameters were functions of the Darcy velocity [35].

Mechanistic insight into macroscale nondilute flow and transport is limited and has been provided solely from laboratory experiments with a limited number of salt species considered. Computational simulations have been performed but are fundamentally flawed as they assume traditional density-dependent macroscale flow and transport equations, which have been shown to be incorrect, can be applied at an already averaged scale (Darcy scale) to gain insight at an even larger scale (macroscale) [36,37]. Furthermore, to simulate transport, the dilute form of Fick's law has been used despite attempting to gain insight on nondilute flow and transport at the macroscale, where Fick's law has been shown to be invalid [6,7,38–40]. From laboratory experiments, we know that the salt species front tends to sharpen as compared to a dilute tracer under the same operating conditions. The sharpness of the salt mass fraction front, in response to a step change in salt mass fraction at the inflow boundary, has been shown

to increase as the incoming mass fraction of the salt species increases. However, if a salt species is initially present in the porous medium, then the difference between the displacing and displaced mass fraction affects the sharpness of the front [6]. For a laboratory data set that used $CaBr_2$, chemical activity effects were found to be significant for constant density difference experiments [6]. Additionally, laboratory experiments show that nondilute displacements produce skewed breakthrough curves and they become more asymmetric as the mass fraction difference between the resident and displacing fluids increases [6]. Mechanistic understanding of these macroscale experimental observations is lacking.

IV. MODEL FORMULATION, APPROXIMATION, AND APPLICATION

A. Microscale model

Fluid flow was modeled at the microscale using the variable-density Navier-Stokes equations [9]. These equations consist of a conservation of mass equation and conservation of momentum equations both of which are written for the fluid phase. The conservation of mass equation is

$$\frac{\partial \rho_w}{\partial t} + \nabla \cdot (\rho_w \mathbf{v}_w) = 0, \tag{1}$$

where ρ_w is the density, t is time, and $\mathbf{v}_w$ is the fluid-phase velocity vector. The conservation of momentum equations for a fluid with variable density and dynamic viscosity are

$$\frac{\partial}{\partial t}(\rho_w \mathbf{v}_w) + \nabla \cdot (\rho_w \mathbf{v}_w \mathbf{v}_w)$$
$$- \nabla \cdot \left\{ \hat{\mu}_w \left[\nabla \mathbf{v}_w + \nabla \mathbf{v}_w^T - \frac{2}{3}(\nabla \cdot \mathbf{v}_w)\mathbf{I} \right] \right\}$$
$$+ \nabla p_{w,rgh} + \mathbf{g}_w \cdot \mathbf{h} \nabla \rho_w = 0, \tag{2}$$

where $p_{w,rgh} = p_w - \rho_w \mathbf{g}_w \cdot \mathbf{h}$, p_w is the pressure of the fluid phase, $\mathbf{h}$ is a position vector of the water surface oriented opposite to the direction of the gravitational vector, $\mathbf{g}^{\overline{w}}$ is the gravitational acceleration vector, $\hat{\mu}_w$ is the dynamic viscosity of the fluid phase, and the superscript T is the transpose operator. Both ρ_w and $\hat{\mu}_w$ are functions of the solution composition for the nondilute case considered. The system is assumed to be isothermal, and the solid phase is immobile.

The microscale species conservation of mass equation is

$$\frac{\partial}{\partial t}(\rho_w \omega_{Aw}) + \nabla \cdot (\rho_w \mathbf{v}_w \omega_{Aw}) - \nabla \cdot (\rho_w D_{Aw} \nabla \omega_{Aw}) = 0, \tag{3}$$

where the qualifier A refers the the salt species, ω_{Aw} is the mass fraction, and D_{Aw} is the diffusion coefficient of species A in the fluid phase. The nondilute diffusion coefficient is approximated as [41,42]

$$D_{Aw} = D_0 \frac{\hat{\mu}_0}{\hat{\mu}_w} \frac{1}{\rho_w V_{Bw}} \left[1 + m_{Aw} \frac{d(\ln \hat{\gamma}_{Aw})}{dm_{Aw}} \right], \tag{4}$$

where D_0 is the dilute diffusion coefficient, $\hat{\mu}_0$ is the viscosity of pure water, V_{Bw} is the partial mass volume of the water (species B), m_{Aw} is the molality, and $\hat{\gamma}_{Aw}$ is the activity coefficient. For a binary system, the Maxwell-Stefan equation and Fick's law are identical [43]. This form of the diffusion coefficient accounts for the concentration dependence that is not

accounted for in the standard Maxwell-Stefan binary diffusion coefficients [44]. Additionally, the activity coefficient appears in the parametrization of the diffusion coefficient to account for that fact that the mass fraction gradient is used as opposed to the chemical potential gradient. At a molecular level, the activity accounts for ionic effects, such as Coulombic interactions and charge balance, as the salt species dissociates into the water phase [45]. The dependence of ρ_w, $\hat{\mu}_w$, and $\hat{\gamma}_{Aw}$ on composition for $CaBr_2$-water solutions were taken from the literature [6].

B. Nondimensional microscale model

The nondimensional form of the governing microscale equations can provide additional insight on the relative importance of each term. Defining the following nondimensional variables:

$$t^* = \frac{v_{in}^w}{d_{50}}t, \quad \mathbf{x}^* = \frac{\mathbf{x}}{d_{50}}, \quad \mathbf{v}_w^* = \frac{\mathbf{v}_w}{v_{in}^w},$$

$$\mathbf{g}_w^* = \frac{\mathbf{g}_w}{G}, \quad \mathbf{h}^* = \frac{\mathbf{h}}{d_{50}}, \quad \nabla^* = d_{50}\nabla, \tag{5}$$

$$\hat{\mu}_w^* = \frac{\hat{\mu}_w}{\hat{\mu}_0}, \quad \rho_w^* = \frac{\rho_w}{\rho_0}, \quad p_{w,rgh}^* = \frac{p_{w,rgh}}{d_{50}\rho_0 G}, \quad D_{Aw}^* = \frac{D_{Aw}}{D_0},$$

where the $*$ superscript refers to a nondimensional quantity, v_{in}^w is the macroscale inlet velocity, d_{50} is the mean grain diameter, and G is the magnitude of the gravity vector. The nondimensional conservation of mass equation for the phase is

$$\frac{\partial \rho_w^*}{\partial t^*} + \nabla^* \cdot (\rho_w^* \mathbf{v}_w^*) = 0, \tag{6}$$

the nondimensional phase momentum equation is

$$\frac{\partial}{\partial t^*}(\rho_w^* \mathbf{v}_w^*) + \nabla^* \cdot (\rho_w^* \mathbf{v}_w^* \mathbf{v}_w^*)$$
$$- \frac{1}{\mathrm{Re}_0} \nabla^* \cdot \left\{ \hat{\mu}^* \left[\nabla^* \mathbf{v}_w^* + \nabla^* \mathbf{v}_w^{*T} - \frac{2}{3}(\nabla^* \cdot \mathbf{v}_w^*)\mathbf{I} \right] \right\}$$
$$+ \frac{1}{\mathrm{Fr}^2}(\nabla^* p_{w,rgh}^* + \mathbf{g}^* \cdot \mathbf{h}^* \nabla^* \rho_w^*) = 0, \tag{7}$$

where

$$\mathrm{Re}_0 = \frac{\rho_0 d_{50} v_{in}^w}{\hat{\mu}_0} \quad \text{and} \quad \mathrm{Fr} = \frac{v_{in}^w}{\sqrt{d_{50}G}}. \tag{8}$$

The nondimensional species mass conservation equation is

$$\frac{\partial}{\partial t^*}(\rho_w^* \omega_{Aw}) + \nabla^* \cdot (\rho_w^* \mathbf{v}_w^* \omega_{Aw})$$
$$- \frac{1}{\mathrm{Pe}_0} \nabla^* \cdot (\rho_w^* D_{Aw}^* \nabla^* \omega_{Aw}) = 0, \tag{9}$$

where

$$\mathrm{Pe}_0 = \frac{d_{50} v_{in}^w}{D_0}. \tag{10}$$

C. Macroscale model

In this work, we are using microscale simulations to investigate dilute and nondilute flow and transport at both the micro- and macroscale. For dilute flow and transport at the

macroscale, well-established models have been developed and consist of macroscale conservation of mass and momentum equations. We assume that the dilute microscale simulations can be modeled as macroscopically one-dimensional systems. All macroscale variables are calculated using their TCAT definitions [9,22].

We summarize the Fickian solute transport model for an immobile and incompressible solid phase for macroscale flow and transport in one spatial dimension, which we denote as z. The macroscale conservation of mass equation for the fluid phase is

$$\frac{\partial (\epsilon^{\overline{\overline{w}}} \rho^w)}{\partial t} = -\frac{\partial}{\partial z}(\epsilon^{\overline{\overline{w}}} \rho^w v^{\overline{w}}), \tag{11}$$

an approximate momentum conservation in the form of Darcy's law is

$$\epsilon^{\overline{\overline{w}}} v^{\overline{w}} = -\frac{\hat{k}}{\hat{\mu}_w} \left(\frac{\partial p^w}{\partial z} + \rho^w g^{\overline{w}} \right), \tag{12}$$

and a species conservation of mass equation for the fluid phase is

$$\frac{\partial (\epsilon^{\overline{\overline{w}}} \rho^w \omega^{A\overline{w}})}{\partial t} = -\frac{\partial}{\partial z}(\epsilon^{\overline{\overline{w}}} \rho^w \omega^{A\overline{w}} v^{\overline{w}}) - \frac{\partial}{\partial z}(\epsilon^{\overline{\overline{w}}} \rho^w \omega^{A\overline{w}} u^{\overline{A\omega}}), \tag{13}$$

where z is positive upwards, $\epsilon^{\overline{\overline{w}}}$ is the porosity, $v^{\overline{w}}$ is the density averaged macroscale fluid velocity in the z direction, $\hat{k}$ is the intrinsic permeability, p^w is the macroscale pressure of the water phase, ρ^w is the macroscale density, which for our work is constant as we are only applying these equations to the dilute simulations, $g^{\overline{w}}$ is the magnitude of the gravitational acceleration, $\omega^{A\overline{w}}$ is the macroscale mass fraction of species A (salt in this work) in the water phase, and $u^{\overline{A\omega}}$ is the macroscale deviation velocity for species A in the water phase.

The deviation velocity for dilute transport is generally parametrized by using a Fickian approximation for the mass flux which can be written as [46]

$$J^{\overline{A\omega}} = \epsilon^{\overline{\overline{w}}} \rho^w \omega^{A\overline{w}} u^{\overline{A\omega}} = -\epsilon^{\overline{\overline{w}}} \rho^w \hat{D} \frac{\partial \omega^{A\overline{w}}}{\partial z}, \tag{14}$$

where $J^{\overline{A\omega}}$ is defined as the mass flux of species A and $\hat{D}$ is the hydrodynamic dispersion coefficient for porous medium systems. The most commonly used form, in one-dimension, is

$$\hat{D} = \frac{\hat{D}_{Aw}}{\hat{\tau}} + \hat{\alpha}_L v^{\overline{w}}, \tag{15}$$

where $\hat{\tau}$ is the tortuosity of the porous medium, which is defined as the average microscale distance traveled by a species per unit macroscale length of the medium and is greater than or equal to one; and $\hat{\alpha}_L$ is the longitudinal dispersivity [46]. It should be noted that this macroscale model is only valid for and applied to the dilute, homogeneous systems at scales above an REV.

D. Model approximations

To solve the microscale model for nondilute flow and transport, a solver was created within the OpenFOAM framework

(v1712) [47]. OpenFOAM is an open-source, finite-volume method, computational fluid dynamics software package that allows for easy parallelization and is packaged with mesh generation software [48]. The existing variable-density Navier-Stokes solvers were not suitable for solving our model as they either couple the density and viscosity through an energy equation as opposed to a species transport equation, lack the necessary gravitational terms, and/or assume constant viscosity.

The governing equations were solved using an implementation of the PIMPLE algorithm [49]. This algorithm is a combination of the semi-implicit method for pressure-linked equations (SIMPLE) algorithm [50] used for steady-state simulations and the pressure implicit with splitting of operators (PISO) algorithm [51,52]. The PIMPLE implementation allows for larger time steps than generally allowed by the CFL condition by iteratively solving the equations and applying under-relaxation. The OpenFOAM solver `rhoPimpleFoam` was used as a template for our model, where we replaced the energy equation with the species transport equation, included the gravitational terms and allowed the density and viscosity to be functions of the salt species mass fraction. To isolate the impacts that the density, viscosity, and activity have on nondilute transport, solvers were also created for models where each of the three functions were forced to equal their dilute value.

To solve the macroscale dilute flow and transport equations, a cell-centered finite-difference code was used [6]. To determine the permeability and longitudinal dispersivity, the method of moving asymptotes algorithm in the software package NLopt (version 2.4.2) [53] was used to minimize the ℓ_2 error norm between the solution to the macroscale equations results and the averaged microscale simulation results.

E. Microscale domain generation

For the microscale simulations, 12/20 Accusand was used as a reference medium to be consistent with the experimental work of Weigand *et al.* [6]. The sphere packing code of Baranau and Tallarek [54] was used to generate sphere pack realizations consistent with the size distribution of the reference medium. With this code, the mean grain diameter ($d_{50} = 0.11$ cm), the standard deviation ($\sigma_{d_{50}} = 0.02$ cm) of the grain diameter, both presented as normal distribution parameters, and the porosity ($\epsilon^{\overline{\overline{w}}} = 0.35$) were matched to the literature values by sampling from a lognormal distribution [55]. The parameters used for the 12/20 Accusand are in agreement with other studies [56].

We examined both a representative elementary volume (REV) scale and a sub-REV-scale. To determine the required domain size for an REV, the intrinsic permeability ($\hat{k}$) and longitudinal dispersivity ($\hat{\alpha}_L$) were calculated for various domain sizes. For each cubic domain, five random sphere packings were generated. When the standard deviation of $\hat{k}$ and $\hat{\alpha}_L$ were less than 5%, we assumed an REV. We found that a domain with a length scale of 9.91 mean grain diameters was sufficient for an REV.

The sub-REV-scale was examined to allow for storage and visualization of the microscale results. Only macroscale variables could be saved for the REV-scale simulations due
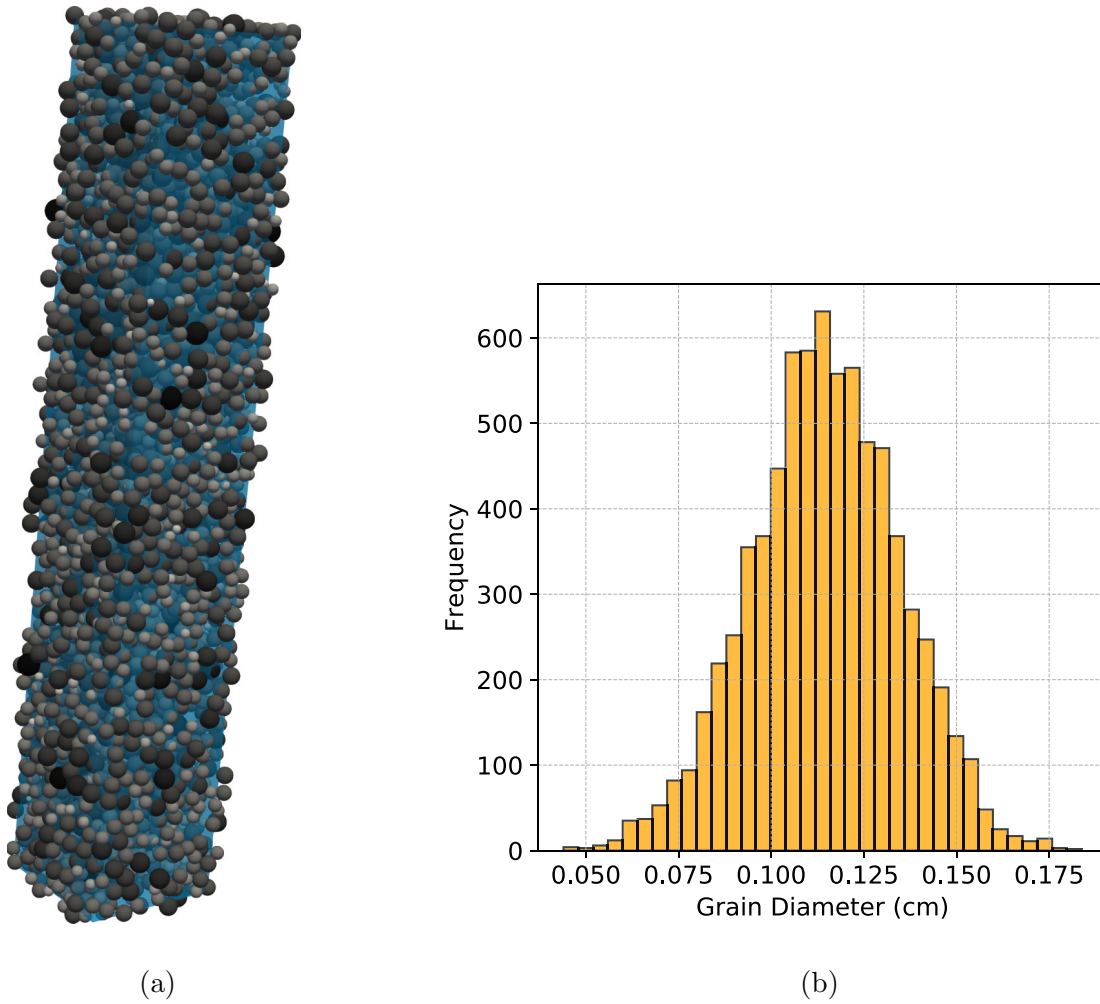
FIG. 1. REV scale domain: (a) sphere pack; and (b) grain diameter distribution with a sample mean of 0.11 cm and standard deviation of 0.02 cm. The direction of flow for all simulations was upwards and the blue box represents the domain that was simulated.

to memory limitations. For the sub-REV simulations, 180 spheres were packed in a cube, with each side equal to 0.514 cm (4.67 mean grain diameters). For the REV simulations, more than 7 400 spheres were packed in a rectangular column, where the height to cross-sectional area had a ratio of 6:1 and the dimensions were 6.54 cm × 1.09 cm × 1.09 cm (59.5 × 9.91 × 9.91 mean grain diameters). This aspect ratio was used to allow for more averaging regions along the direction of flow while still having a large enough cross section to ensure a REV.

The distributions and packed media are shown in Figs. 1 and 2 for the REV-scale and sub-REV-scale, respectively. The porosity for both of the domains was 0.35. The tortuosity was calculated for the sub-REV domain using [57,58]

$$\tau = \frac{\int |\mathbf{v}_w| dx}{\int v_z dx}, \tag{16}$$

where v_z is the velocity in the main direction of flow.

F. Model implementation

The sphere-packing code provided sphere centroids and radii that were discretized in OpenFOAM using

snappyHexMesh. snappyHexMesh is a mesh generation software package that takes a structured Cartesian grid and generates an unstructured mesh that approximately conforms to the specified surface geometries. The user has the ability to control the reconstruction of the geometry through the integer-valued refinement parameter, which specifies how to split the cells of the structured grid near a specified surface. For example, a surface refinement level of one splits one structured grid cell near the refinement surface into four new cells. The work of Icardi *et al.* [13] found a refinement level of 2 in snappyHexMesh was sufficient to produce a solution that was grid independent; however, only the flow field was examined and not species transport. To confirm their conclusions and ensure the salt species was also independent of the grid for our simulations, a grid independence study was performed on the sub-REV domains. We found a strong dependency on the structured grid that must be supplied before the mesh is refined around the solid grains but a refinement level of 2 was sufficient. The final mesh for the sub-REV domains consisted of 9.28×10^5 cells.

For the microscale simulations, wall boundary conditions were assumed for the sides of the packed column, where the sides are specified as the direction orthogonal to gravity.
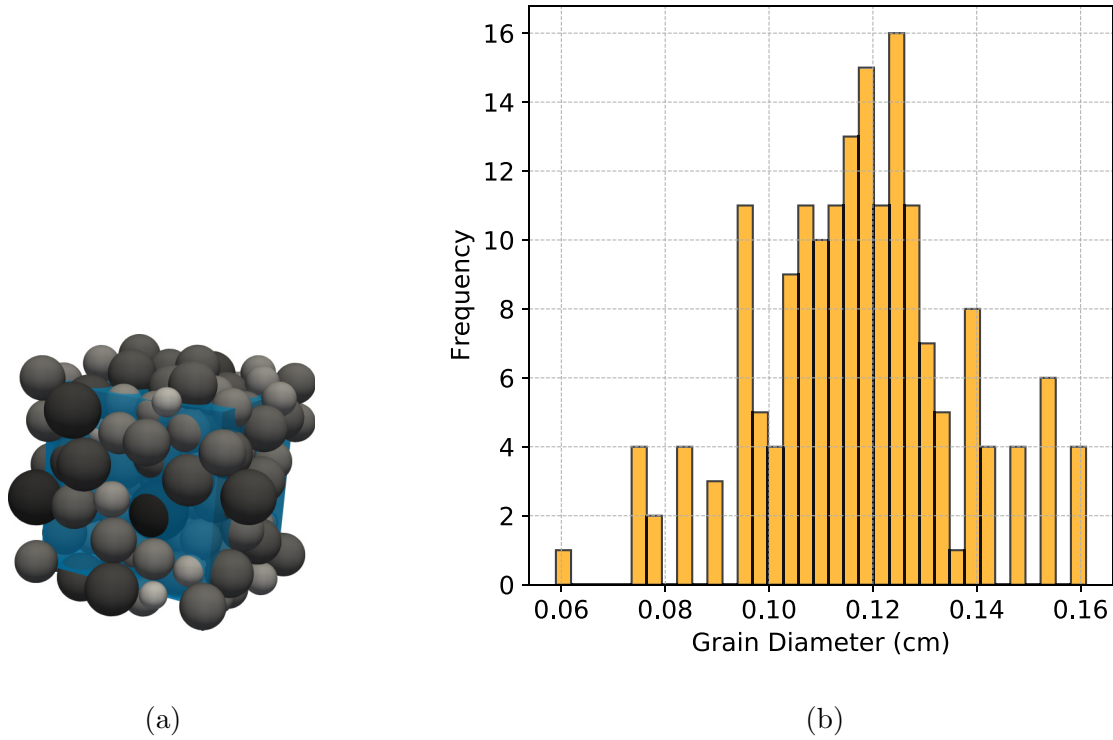
FIG. 2. Sub-REV domain: (a) sphere pack; and (b) grain diameter distribution with a sample mean of 0.12 cm and standard deviation of 0.019 cm. The blue box represents the domain that was simulated.

At the top of the column, outflow boundary conditions were specified, which fixed the pressure to atmospheric pressure and forced a zero gradient for the velocity and salt mass fraction. For the inlet boundary condition, a fixed mass flow rate was enforced for all simulations, and the incoming salt mass fraction was constant. By using a fixed mass flow rate, the volumetric flow rate, and in turn the macroscale velocity, varied because the density of the incoming fluid depended upon salt mass fraction.

The simulations performed consisted of varying the incoming salt mass fraction (ω_{in}), the salt mass fraction initially present in the column (ω_{res}), and the incoming mass flow rate. For the initial conditions, the steady-state incompressible and constant density Navier-Stokes equations were solved based on the resident fluid properties and the resulting pressure and velocity fields were used as the initial conditions for the transient simulations. This was done so that the system began with a fully developed flow field.

Macroscale averages were calculated on the fly for the REV-scale simulations as the microscale data could not be stored due to memory limitations. The macroscale averages were calculated according to Refs. [9,22]. The domain was split into seven different overlapping REVs and macroscale average values were calculated in each volume. Each REV contained the entire cross-section of the domain and had a height in the direction of flow of 3.27 cm. The REVs overlapped by 0.545 cm. Additionally, averaged microscale values were calculated at seven different cross sections along the height of the column separated by a distance of 1.09 cm. For the sub-REV simulations, all data could

be stored however microscale averages were also calculated for five different volumes and at eight different cross sections.

For the salt species, calcium bromide ($CaBr_2$) was selected due to the complex nature of its activity coefficient and its use in previous studies. The density, viscosity, and activity coefficients from Weigand *et al.* [6] were used. The dilute diffusion coefficient (D_0) was set to $1.05 \times 10^{-5} \, cm/s^2$.

The REV scale simulations were run with OpenFoam v1712 on UNC Research Computings Dogwood cluster with 2 107 processors. OpenFOAM's implementation of Scotch was used for domain decomposition [59]. For the sub-REV-scale simulations, the number of processors changed to four.

V. RESULTS AND DISCUSSION

A. Dilute simulations

1. Dilute REV-scale simulations

Dilute simulations at three different mass flow rates ($\dot{m}_{in}^{w}$) were first performed so that a baseline could be established to allow for comparisons between dilute and nondilute flow and transport. The dilute simulations also allowed us to characterize the porous media to ensure that the model produced expected behavior for the media being simulated.

The microscale simulation results were averaged and the resulting macroscale breakthrough curve was used to determine the longitudinal dispersivity ($\hat{\alpha}_L$). This was accomplished by performing a parameter estimation where the dilute macroscale flow and transport equation was fit to the
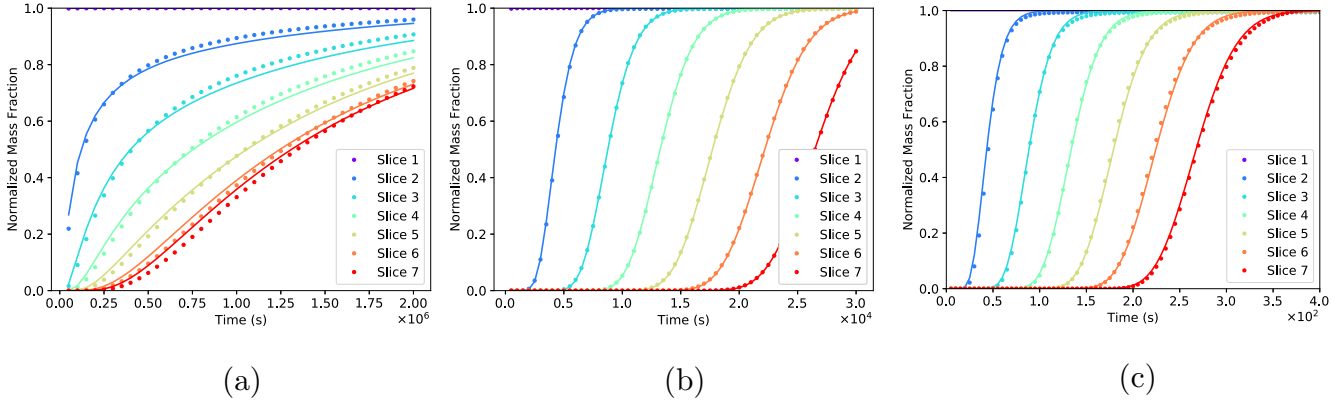
FIG. 3. Results of fitting the dilute macroscale model (lines) to REV-scale cross-section averaged microscale data (points) for Pe $= 0.026$ (a), 2.6 (b), and 260 (c).

averaged microscale results at a cross-section by optimizing the longitudinal dispersivity, as shown in Fig. 3. The first two averaging regions were excluded from the fits to avoid any entrance effects. To determine the intrinsic permeability of the porous media ($\hat{k}$), Eq. (12) was used with the averaged microscale results for fluid pressure at the inlet and outlet of the domain. The sub-REV-scale domain dilute simulation results were used with Eq. (16) to estimate a value of the tortuosity of 1.22, which agrees with the literature [13,14]. This value was used for the dilute macroscale transport equation.

The conditions and resulting estimated parameters for three dilute simulations performed at an REV-scale are reported in Table I. The $\hat{\alpha}_L$ reported by Weigand *et al.* [6] for a similar medium ranged from 0.098–0.16 cm and were based on laboratory experiments. The increase of the dispersivity for the highest Pe_0 agrees with the literature [13]; the Re_0 also increases and offers a mechanistic rationale for this observation. Schroth *et al.* [56] report an intrinsic permeability of 4.6×10^{-6} cm^2 for 12/20 Accusand, which is slightly lower than our estimated value, however they also report different mean grain diameters and porosities than used in this work, and spheres are an idealized representation of Accusand.

2. Dilute Sub-REV-scale simulations

To assess how the microscale velocity distribution impacts macroscale dispersion, sub-REV-scale dilute simulations were performed for a set of Re_0 that matched the REV-scale

TABLE I. Experimental values and optimized macroscale parameters for the REV-scale dilute simulations.

$\dot{m}_{in}^{w}$ (g/s)	Re_0	Pe_0	$\hat{\alpha}_L$ (cm)	$\hat{k}$ (cm^2)
10^{-6}	3.1×10^{-5}	0.026	0.049	7.4×10^{-6}
10^{-4}	3.1×10^{-3}	2.6	0.035	7.4×10^{-6}
10^{-2}	3.1×10^{-1}	260	0.15	7.4×10^{-6}

simulations. Complete microscale simulation details were stored and analyzed for the sub-REV-scale simulations.

The sub-REV-scale velocities were sampled along cross-sections orthogonal to the direction of flow near the outflow boundary ($z = 0.513$). Figure 4 shows the distribution of the microscale velocity components for the lowest and highest Re_0 for the sub-REV domain. For all three simulations, the means of the velocities in direction orthogonal to the flow (v_x and v_y) are approximately zero. For the velocity in the direction of flow, the mean is equal to the superficial face velocity. This agrees with Aramideh *et al.* [14]; however, Icardi *et al.* [13] stated that the bin with the highest frequency corresponded to their superficial velocity. This suggests an error in their results as the density weighted mean of the velocity in the direction of flow must equal the superficial velocity. Additionally, the mean and standard deviation for the velocity in the z direction are equal. Aramideh *et al.* [14] showed that the microscale velocity distribution at low porosities are nearly exponentially distributed. To test this, the velocity in the z direction was fit to an exponential distribution but failed both the Kolmogorov-Smirnov and Andersen-Darling goodness-of-fit tests [60].

The microscale velocities in the mean direction of flow are all positive for every flow rate considered. Icardi *et al.* [13] observed negative velocities at similar Re_0 but their porous media consisted of irregular and polydisperse objects that contained local blockages that resulted in the negative velocities in the mean direction of flow. The work of Aramideh *et al.* [14] examined mono- and polydisperse spheres and while they observed negative velocities at similar Re_0, they considered it to be negligible. For nondilute flow and transport, negative velocities in the mean direction of flow can develop due to gravity stabilization; however, for dilute flow and transport they represent recirculation zones. Since we did not observe any negative velocities in our dilute simulations, if we observe negative velocities in the mean direction of flow in our nondilute simulations, then they can be attributed to gravity stabilization effects. The velocity distributions and ranges for the three simulations are nearly identical but scaled. This shows that, with the Re_0 considered, no new flow pathways are forming [61].
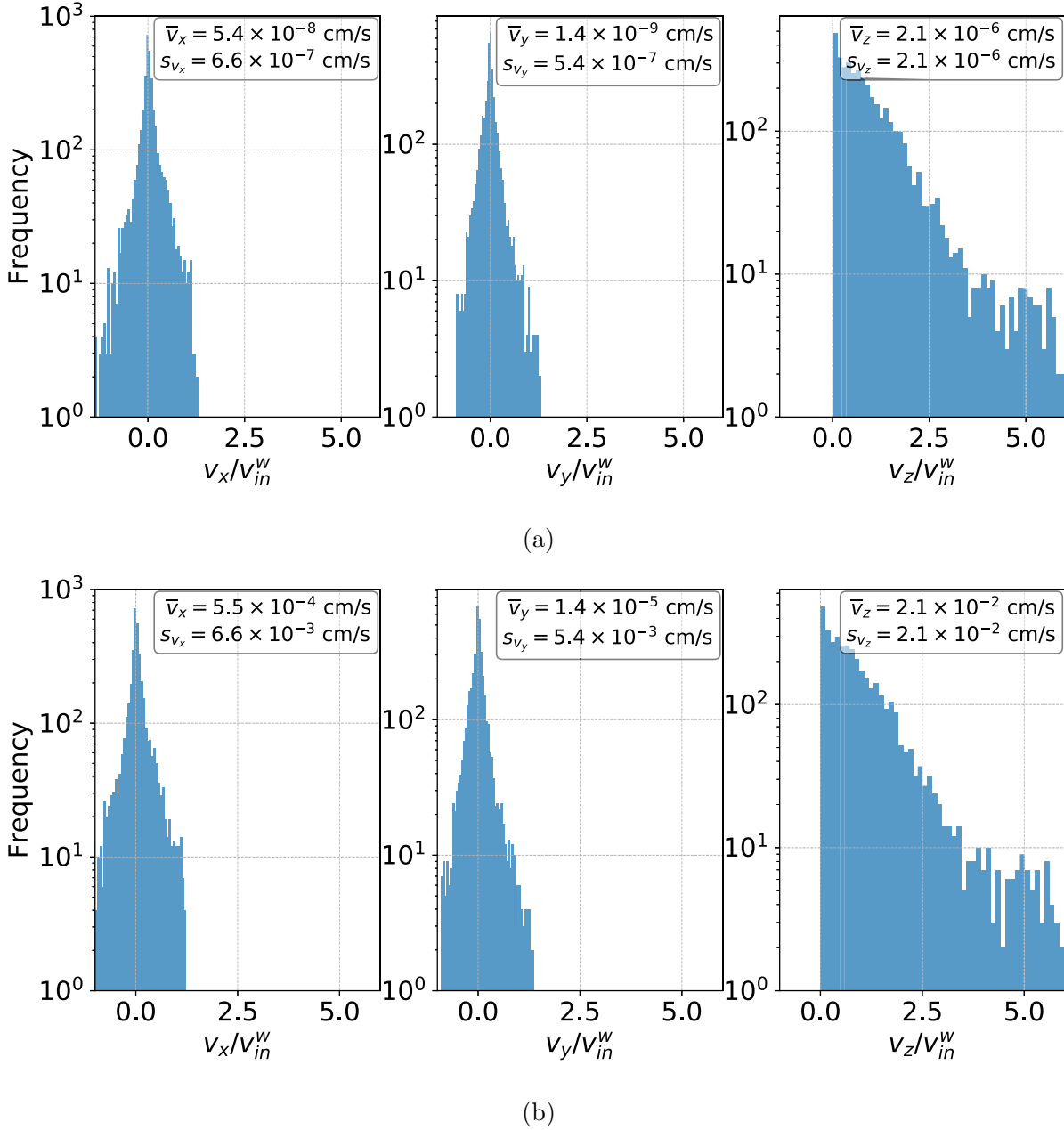
FIG. 4. Dilute microscale sub-REV velocity distributions for $\mathrm{Re}_0 = 3.1 \times 10^{-5}$ (a) and $\mathrm{Re}_0 = 0.31$ (b). The means and standard deviations of the velocity are included. The distributions were sampled at a cross-section orthogonal to the mean direction of flow.

B. Nondilute

1. Nondilute REV-scale simulations

The laboratory work by Weigand *et al.* [6] consisted of a single incoming flow rate that had a Re_0 of 0.07. While we did not directly match that Reynolds number, Fig. 5 shows the macroscale mass fraction breakthrough curves for our most similar set of simulations ($\mathrm{Re}_0 \approx 10^{-1}$). The length of the column in the laboratory experiments was more than 10 times longer than the REV-size domains for the microscale simulations. We observe that the averaged microscale results follow the same trend as the experimental data. The dilute model produces the most disperse solution and the breakthrough curve sharpens as the incoming mass fraction increases, while the

resident initial condition fluid mass fraction remains zero. For the simulation with a nonzero resident initial condition salt mass fraction, the averaged microscale simulation results also show breakthrough curve profiles similar to those previously reported based upon laboratory studies despite the slightly different mass fractions used.

The REV-scale nondilute simulations were performed at the same three mass flow rates that were used with the dilute microscale simulations and five different combinations of initial mass fractions and displacing mass fractions for the salt species were examined for each flow rate. For the nondilute simulations, the Re and Pe vary throughout the domain as the densities, viscosities, and diffusion coefficient are functions of the mass fraction. We define these numbers, as well as
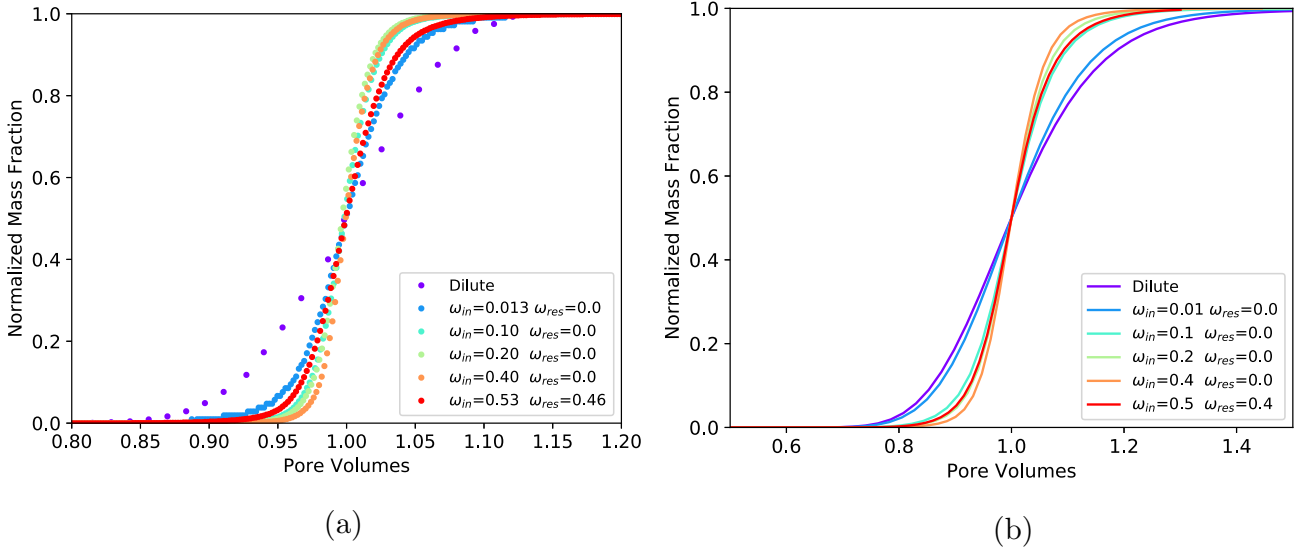
(a)

(b)

FIG. 5. Nondilute species breakthrough curves: (a) laboratory experiments from [6]; and (b) averaged REV-scale microscale simulations.

a nondimensional gravity number (N_g) and a viscosity ratio ($M_{\hat{\mu}}$) to aid interpretation of the simulated results as

$$\mathrm{Re} = \frac{\rho_{\mathrm{in}} d_{50} v_{\mathrm{in}}^w}{\hat{\mu}_{\mathrm{in}}}, \qquad (17)$$

$$\mathrm{Pe} = \frac{d_{50} v_{\mathrm{in}}^w}{D_{Aw,\mathrm{in}}}, \qquad (18)$$

$$N_g = \frac{(\rho_{\mathrm{in}} - \rho_{\mathrm{res}})\hat{k}G}{\hat{\mu}_{\mathrm{in}} v_{\mathrm{in}}^w}, \quad \text{and} \qquad (19)$$

$$M_{\hat{\mu}} = \frac{\hat{\mu}_{\mathrm{res}}}{\hat{\mu}_{\mathrm{in}}}. \qquad (20)$$

N_g is a measure of the ratio of gravitational forces to advective forces. For large N_g, gravity stabilization becomes dominant compared to advective transport. $M_{\hat{\mu}}$ in this work will always be $\leqslant 1$ as we only consider viscous-stable displacements. For small viscosity ratios, viscous stabilization effects may become important. Table II shows the Re, Pe, N_g, and $M_{\hat{\mu}}$ for the two highest mass flow rate simulations. The decrease in the Re and Pe as the incoming mass fractions increase is due to a decrease in the inlet velocity.

The breakthrough curves for Re $\approx 10^{-3}$ simulations are shown in Fig. 6. The breakthrough curves for Re $\approx 10^{-5}$ (not

shown) only differ from the Re $\approx 10^{-3}$ curves in that the solutions are more diffuse, and the displacement simulation where $\omega_{\mathrm{in}} = 0.1$ is more diffuse than the dilute displacement at the lowest flow rate. These simulations depict behavior that is in contrast to the current understanding of macroscopic nondilute transport. The front is thought to sharpen as the incoming mass fraction increases but we observe the opposite behavior at these Pe [7,8,37,39,40,62–64]. The molecular diffusion coefficient as a function of mass fraction is shown in Fig. 7. The sharpness of the nondilute fronts is correlated to the diffusion coefficient with one exception. For the case where $\omega_{\mathrm{in}} = 0.1$, the diffusion coefficient is slightly larger (2%) than the dilute diffusion coefficient and the Pe is slightly lower than the dilute displacement, however, the nondilute displacement breakthrough is sharper than the dilute breakthrough curve. This demonstrates that we are observing nondilute behavior for these displacement simulations as a higher diffusion coefficient and lower Pe should produce a

TABLE II. Nondilute REV-scale simulation parameters for the two highest mass flow rates considered. The two highest flow rate simulations have Re $\approx 10^{-3}$ and Re $\approx 10^{-1}$, respectively.

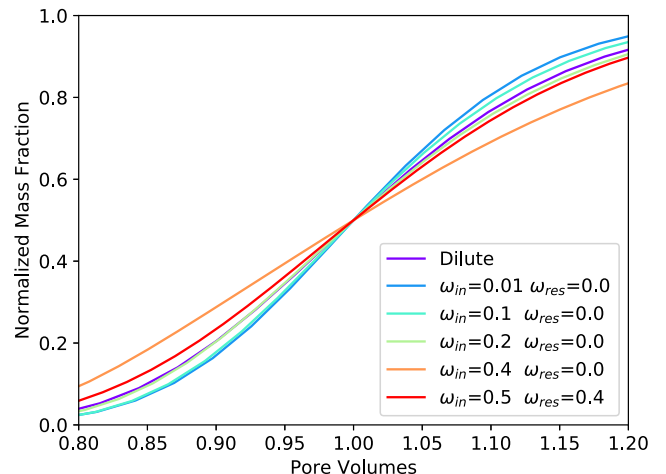| ω_{in}	ω_{res}	$\dot{m}_{\mathrm{in}}^w = 10^{-4}$ g/s				$\dot{m}_{\mathrm{in}}^w = 10^{-2}$ g/s			
		Re (10^{-3})	Pe	N_g	$M_{\hat{\mu}}$	Re	Pe	N_g	$M_{\hat{\mu}}$
Dilute	0	3.1	2.6	0	1.00	0.31	260	0	1.00
0.01	0	3.0	3.1	81	0.99	0.30	310	0.81	0.99
0.1	0	2.7	2.3	840	0.89	0.27	239	8.4	0.89
0.2	0	2.4	1.6	1800	0.78	0.24	160	18	0.78
0.4	0	1.3	0.99	2900	0.43	0.17	99	29	0.43
0.5	0.4	0.73	0.99	2500	0.55	0.073	99	25	0.55

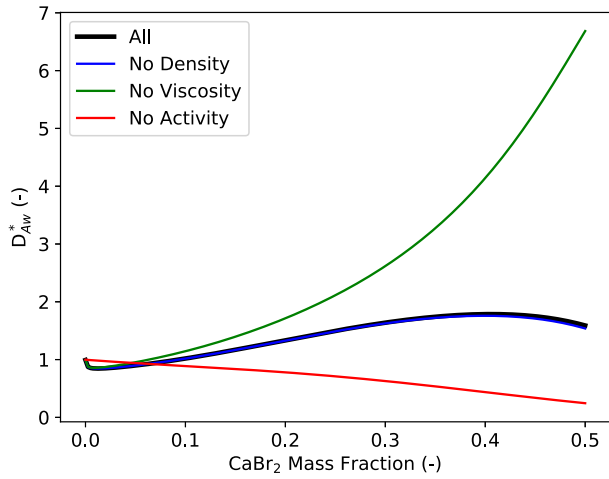FIG. 6. Averaged REV-scale nondilute breakthrough curves for Re $\approx 10^{-3}$.

FIG. 7. Molecular diffusion sensitivity to density, viscosity, and activity [see Eq. (4)].

more diffuse breakthrough curve for a dilute displacement simulation.

The macroscale breakthrough curves for $Re \approx 10^{-1}$ are shown in Fig. 5(b). This set of simulations is in good agreement with existing experimental work and the current understanding of nondilute behavior [6–8,65]. The curves sharpen as the incoming mass fraction increases and when the resident fluid has a nonzero salt concentration, the difference between the fluid properties controls behavior. At this high of a Pe number, the nondilute behavior is a result of the nondilute effects on the flow field. While molecular diffusion will

still impact the solution, it becomes a higher order effect as can be seen with the $\omega_{in} = 0.4$ simulation having the highest molecular diffusion coefficient but also having the sharpest breakthrough curve at this flow rate.

2. Nondilute sub-REV simulations

As was done with the dilute simulations, sub-REV simulations were performed to examine microscale behavior. Figure 8 shows the normalized microscale mass fractions at a cross-section along the mean flow direction for the dilute tracer and for the $\omega_{in} = 0.4$ displacement simulation at $Re \approx 10^{-3}$, where flow is moving upwards. The $\omega_{in} = 0.4$ displacement simulation was more disperse than the dilute simulation at this Re due to diffusion coefficient that was 1.79 times larger than the dilute diffusion coefficient.

The mixing zone was determined by computing the density weighted average of the salt mass fraction computed over the area normal to the mean direction of flow and defined as the bounds on z for which the normalized salt mass fraction was in [0.001,0.999]. The upper bound defined the trailing edge and the lower bound the leading edge (Fig. 9). The mixing zone thickness was found by subtracting the leading edge location from the trailing edge location.

By examining the microscale mass fractions, we can see the effects of gravity stabilization. For the dilute case, the salt concentration varies significantly in any given cross-section in the mixing zone orthogonal to the direction of flow. This is due to mechanical dispersion. For the nondilute simulation, there is less variation in the mass fraction. Figure 10 shows the variance of the normalized mass fraction over time at a cross-section orthogonal to the direction of flow near the
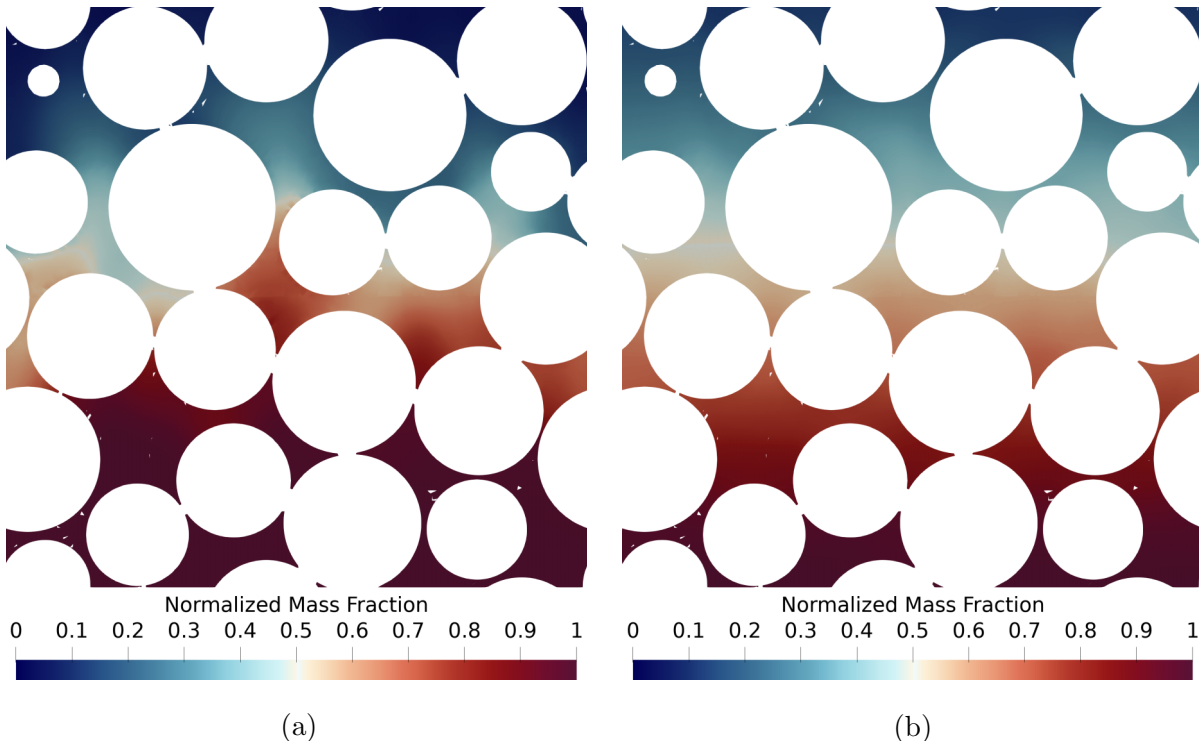

FIG. 8. Normalized microscale mass fraction simulations at $Re \approx 10^{-3}$ for an upward flow displacement pattern: (a) dilute case; and (b) $\omega_{in} = 0.4$ and $\omega_{res} = 0$.
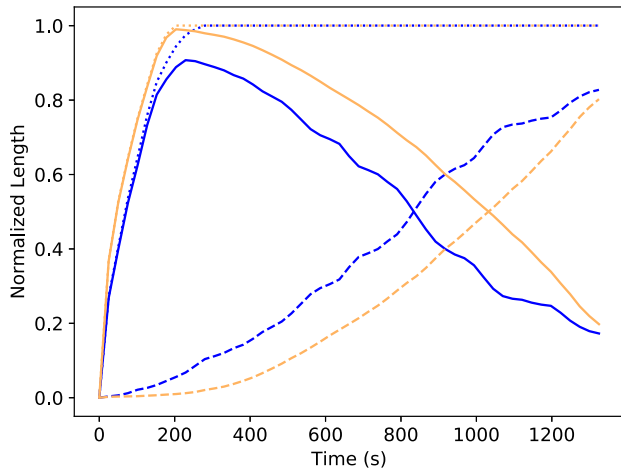
FIG. 9. Leading edge (dotted line) and trailing edge (dashed line) of the mixing zone, and the mixing zone thickness (solid line) for the dilute (blue) and $\omega_{in} = 0.4$ and $\omega_{res} = 0$ (yellow) simulations at Re $\approx 10^{-3}$.

outlet. When a denser fluid is above a less dense fluid, which can be caused by the tortuous path of a porous media, gravity will force the denser fluid downwards. This results is a more uniform mass fraction distribution in the direction of flow and counteracts mechanical dispersion. However, as seen in Fig. 9, the nondilute ($\omega_{in} = 0.4$) mixing zone is larger than the dilute mixing zone at this Re. The macroscale breakthrough curves for the dilute simulation and $\omega_{in} = 0.1$ and $\omega_{res} = 0$ simulation are similar (Fig. 6) and have nearly identical diffusion coefficients, however the variance is greatly reduced for the nondilute simulation. This shows that gravity stabilization is impacting the microscale mass fraction distribution but the macroscale breakthrough curves are relatively insensitive to gravity stabilization at this Pe and are governed by the variable diffusion coefficient.

By examining the nondimensional form of the variable-density Navier-Stokes equation [Eq. (7)], the relative importance of each term can be observed. For the nondilute
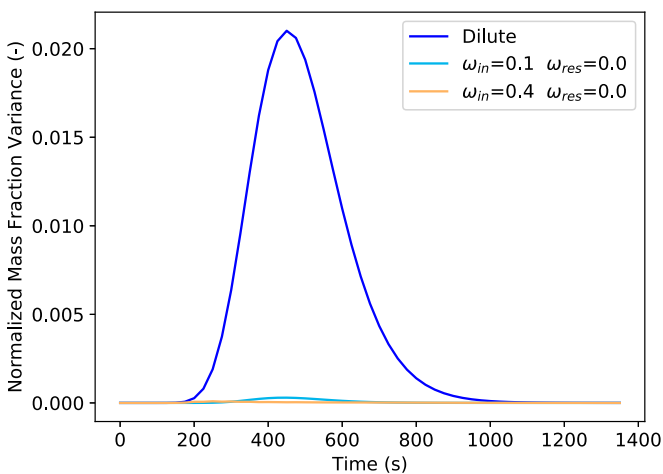

FIG. 10. Normalized mass fraction variance averaged over a plane located at $z = 0.513$ for dilute and nondilute simulations at Re $\approx 10^{-3}$.

displacement with $\omega_{in} = 0.4$, Re^{-1} is 7.6×10^2 and Fr^{-2} is 4.2×10^8; therefore, the dominant term in Eq. (7) is the term with the Fr. Ignoring all other terms, the gradient of the pressurelike term ($p^*_{w,rgh}$) and the density must be approximately equal, as gravity is assumed constant in this work, but have opposite signs. When a more dense fluid is above a less dense fluid, the gradients of the pressure and density have the same sign. This can produce either negative velocities in the direction of gravity or slow down the velocities in the mean direction of flow. This stabilization restricts the movement of the salt species and produces a more uniform microscale mass fraction field along a given cross-section orthogonal to gravity.

To further examine the effects of gravity stabilization, the microscale velocities and mass fractions were sampled at a cross-section orthogonal to the gravitational vector (Fig. 11). For our dilute microscale simulations, no negative velocities in the direction of gravity were observed at the Reynolds numbers considered. For our nondilute simulations, we observe negative velocities that are a result of gravity stabilization. The velocity distribution in the mean direction of flow becomes increasingly more skewed to the left as the incoming salt mass fraction increases, resulting in larger negative velocities. The variance of the velocity components orthogonal to gravity (v_x and v_y) increases as the salt front passes through as compared to the dilute simulations. Gravity stabilization not only impacts the velocities in the direction of gravity but also the velocities orthogonal to gravity as gravity acts to stabilize the front.

The same sub-REV analysis was performed for the simulations with Re $\approx 10^{-1}$ and the normalized microscale mass fractions for the dilute and $\omega_{in} = 0.4$ displacement simulation are shown in Fig. 12 and the leading and trailing edges of the mixing zone and mixing zone thickness are shown in Fig. 13. As with the lower Re simulations, the nondilute displacements result in a lower variance of the normalized mass fraction at a given cross-section orthogonal to flow as compared to the dilute simulation (Fig. 14). Mechanical dispersion increases with fluid velocity, and at this Re we observed increased mechanical dispersion and increased variance in the mass fractions for the dilute and nondilute simulations as compared to the lower Re simulations. However, the length of the mixing zone is shorter for the nondilute simulations as compared to the dilute tracer, which produces a sharper macroscale breakthrough curve for the nondilute system.

At this larger Re, however, we observe locations where a higher density fluid is above a lower density fluid, which was not observed for the lower Re simulations. Comparing the gravity numbers for the $\omega_{in} = 0.4$ displacement simulations at the two different Re shows that at the larger Re simulation, gravitational to viscous forces are reduced by two orders of magnitude at the larger Re compared to the small Re, which results in regions in which instabilities remain for the larger Re case. This results in an increase in the mass fraction variation at a cross-section aligned with the mixing zone. Comparing Figs. 10 and 14 shows the increase of the mass fraction variance at the higher Re number simulations for both the dilute and nondilute simulations. For the $\omega_{in} = 0.4$ simulation, $Re^{-1} = 7.6$ and $Fr^{-2} = 4.2 \times 10^5$, which means the Fr term is still dominating behavior.
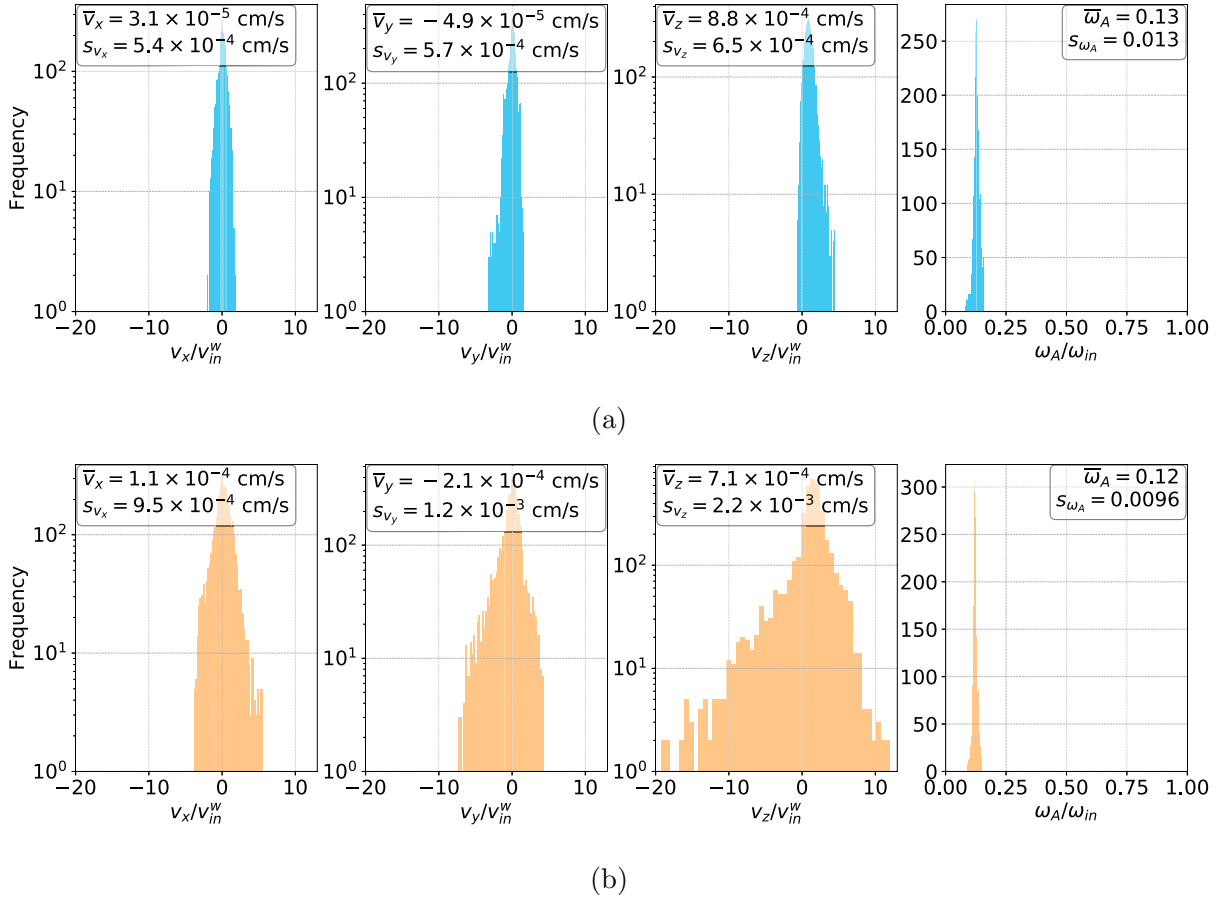
FIG. 11. Distribution of velocity components and mass fraction sampled for a cross-section at $z = 0.513$ for simulations at Re $\approx 10^{-3}$: (a) $\omega_{\text{in}} = 0.1$; and (b) $\omega_{\text{in}} = 0.4$.

To confirm these observations, the nondilute microscale velocity distributions at a cross-section near the outlet ($z = 0.513$) at the largest Re are shown in Fig. 15. No negative velocities are observed in the direction of gravity for the nondilute displacements at this Re. However, the variance in the velocity decreases as compared to the dilute simulation at this Re [Fig. 4(b)], and the relatively large positive velocities in the direction of flow no longer occur. For the nondilute displacement with $\omega_{\text{in}} = 0.4$, the standard deviation of the velocity in the z direction has a minimum value of 0.043 cm/s and occurs when the front is approximately halfway through the domain. For the lower Re simulations, the standard deviation of v_z increased as the front moved through the domain. For the lower Re simulations, where the gravity numbers are two orders of magnitude larger, uniformly stable distributions were observed, which was not the case at higher Re.

The distribution of the mass fraction at the higher Re simulations is also skewed (Fig. 15), which from a macroscale perspective produces a breakthrough curve that is asymmetric. This macroscale behavior has been observed by Weigand *et al.* [6] and was attributed to activity effects but this does not seem to be true as the lower Re simulations would also have a skewed or asymmetric distribution at the microscale. We attribute the asymmetry to the nonlinear density function. As the mass fraction increases so does the density gradient.

Therefore, gravitational stabilization affects higher mass fractions more than lower mass fractions, which can be seen from the gravity number. This explains the skewness in the mass fraction histogram as well as the observed increase in size of negative velocities as the mass fraction increases at lower Re.

C. Isolation of phenomena

One of the benefits of computational simulations over laboratory experiments is the ability to isolate different phenomena. Figures 16 and 17 show the REV-scale macroscale breakthrough curves for Re $\approx 10^{-3}$ and Re $\approx 10^{-1}$, respectively, where we independently set the activity, density, and viscosity such that they are no longer functions of the salt species and are equal to their dilute values. For the simulations where the resident fluid had a nonzero salt mass fraction, we fixed the density and viscosity to the values that correspond to the resident salt mass fraction.

1. Activity

Activity only appears in the molecular diffusion coefficient and when we neglect activity effects, the molecular diffusion coefficient monotonically decreases as the mass fraction increases (Fig. 7). For the nondilute simulations with Re $\approx 10^{-3}$, the macroscale breakthrough curves were correlated to
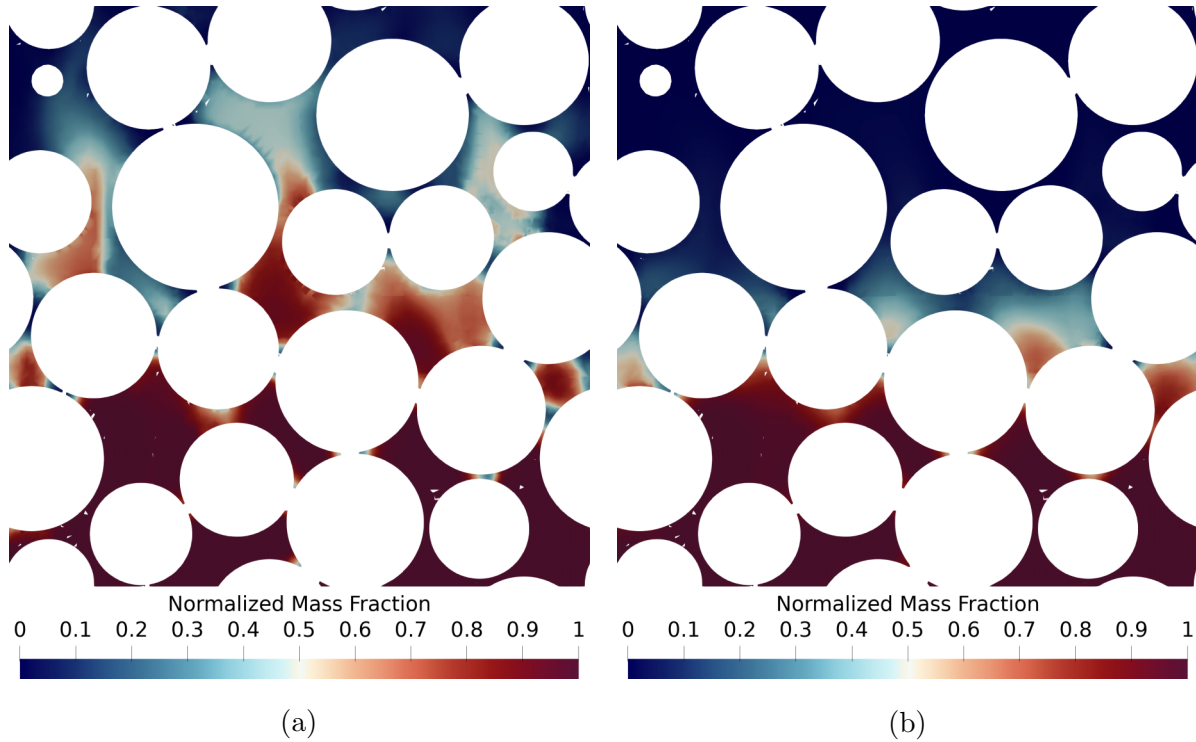
FIG. 12. Normalized microscale mass fraction simulations at Re $\approx 10^{-1}$ for an upward flow displacement pattern: (a) dilute case; and (b) $\omega_{\text{in}} = 0.4$ and $\omega_{\text{res}} = 0$.

the diffusion coefficient with the exception of the simulation with $\omega_{\text{in}} = 0.1$, which was sharper than could be described by just examining the diffusion coefficient and Pe. Additionally, by examining the microscale flow field, we observed gravitational stabilization effects that produced negative velocities for the nondilute simulations at this flow rate.

When the activity is turned off for the simulations with Re $\approx 10^{-3}$, every breakthrough curve sharpens with the exception of the $\omega_{\text{in}} = 0.01$ because the diffusion coefficient increases when activity is turned off. The changes in the

macroscale curves are more significant for the higher mass fraction displacements where the variable diffusion coefficient is more sensitive to activity. For the higher Re simulations (Fig. 17), the macroscale behavior is insensitive to activity effects, which results in the breakthrough curves being essentially identical for the simulations with all effects included and those in which activity was ignored.

At higher Re and Pe numbers, activity is a higher-order phenomena for macroscale nondilute transport. At the lower Re and Pe, activity only becomes important at high mass fractions. The activity coefficient for CaBr$_2$ is highly nonlinear
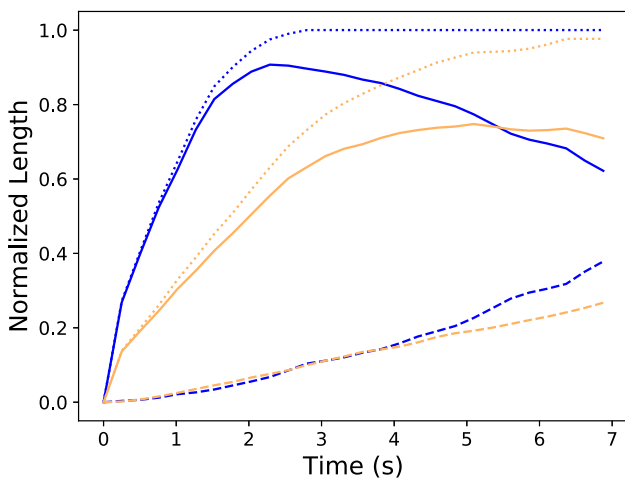

FIG. 13. Leading edge (dotted line) and trailing edge (dashed line) of the mixing zone, and the mixing zone thickness (solid line) for the dilute (blue) and $\omega_{\text{in}} = 0.4$ and $\omega_{\text{res}} = 0$ (yellow) simulations at Re $\approx 10^{-1}$.
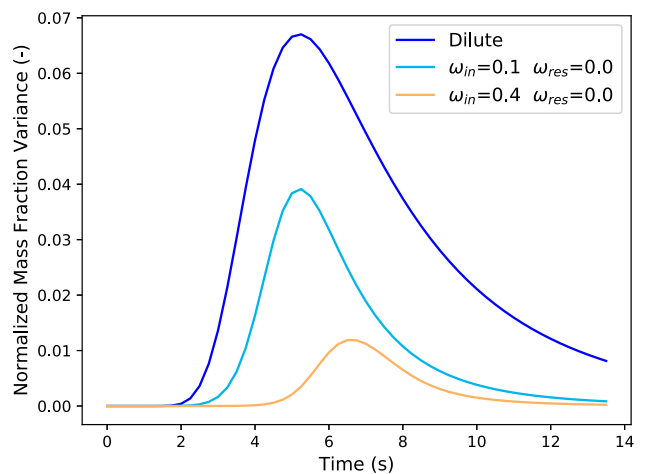

FIG. 14. Normalized mass fraction variance averaged over a plane located at $z = 0.513$ for dilute and nondilute simulations at Re $\approx 10^{-1}$.
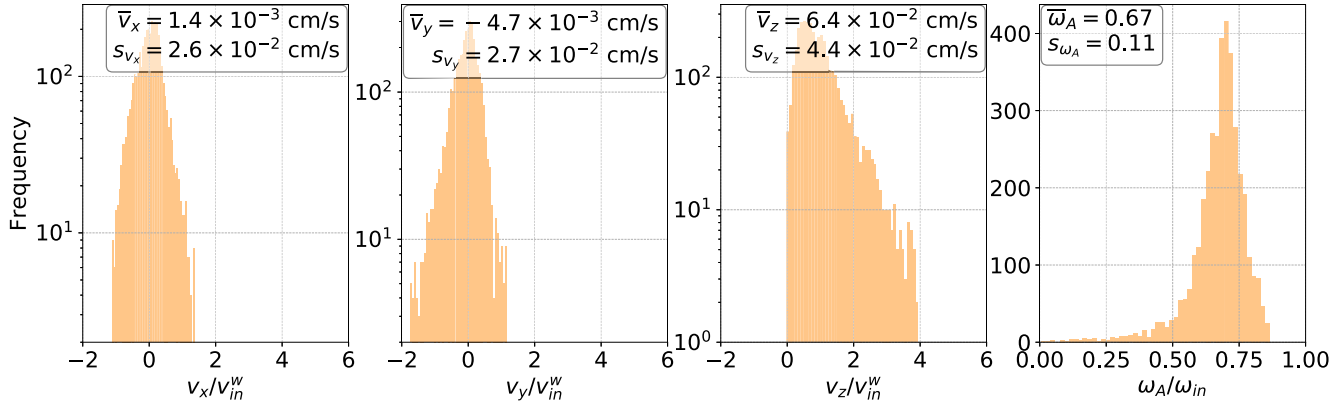
FIG. 15. Distribution of velocity components and mass fraction sampled for a cross-section at $z = 0.513$ for simulations at Re $\approx 10^{-1}$ and $\omega_{in} = 0.4$.

and increases exponentially at high mass fractions. For other salt species such as NaCl, the activity coefficient does not increase as significantly and is likely to be unimportant for essentially all conditions.

2. Viscosity

Not only does the viscosity appear in the microscale conservation of momentum equation, but it also appears in the molecular diffusion coefficient. With the viscosity turned off, the molecular diffusion coefficient increases as the mass fraction increases (Fig. 7). Additionally, with no viscosity gradient, viscous stabilization that sharpens macroscale breakthrough curves cannot occur [62]. However, if we examine the nondimensional form of the Navier-Stokes equation, then we see that the viscosity appears in a term that is multiplied by the Re^{-1}. From our previous analysis, we expect viscosity to be a higher order effect as the term associated with Fr^{-2} is dominant. The viscosity is also in the denominator in the gravity number. A decrease in the viscosity, increases

the gravity number—increasing the ratio of gravitational to viscous forces.

As stated, at the lower Re and Pe, the nondilute simulations are controlled by the molecular diffusion coefficient. Every breakthrough curve at the lower Re is more disperse when viscous effects are neglected and the higher the incoming mass fraction, the more disperse the breakthrough curve. The viscosity function for CaBr$_2$ is an exponential function so it is expected to see the most dramatic impacts at the higher mass fractions.

For the highest Re simulations, the viscosity impacts on the macroscale breakthrough curve are negligible. The microscale velocity distribution with a fixed viscosity is nearly identical to the microscale velocity distribution with a variable viscosity. The flow profile is relatively insensitive to the viscosity due to the choice of a fixed incoming mass flow rate boundary condition. The pressure does increase when the viscosity is variable and minor changes in the velocities are observed in the pore throats but they do not change enough to impact significantly macroscale transport.
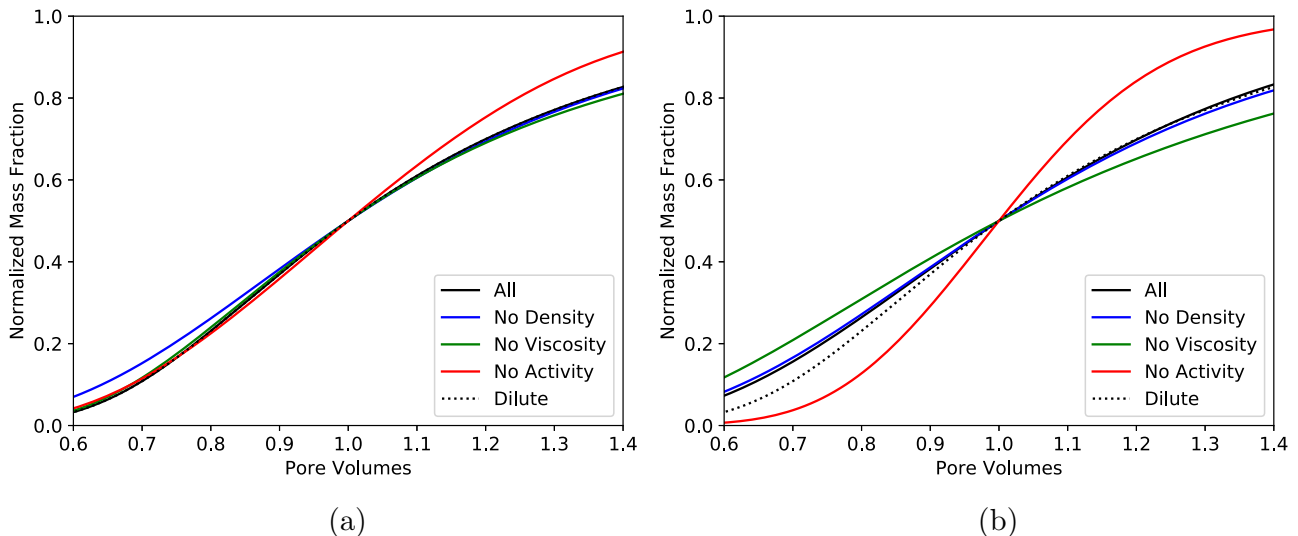

(a)

(b)

FIG. 16. Sub-REV-scale breakthrough curve sensitivity at Re $\approx 10^{-3}$: (a) $\omega_{in} = 0.4$ and $\omega_{res} = 0$; and (b) $\omega_{in} = 0.5$ and $\omega_{res} = 0.4$.
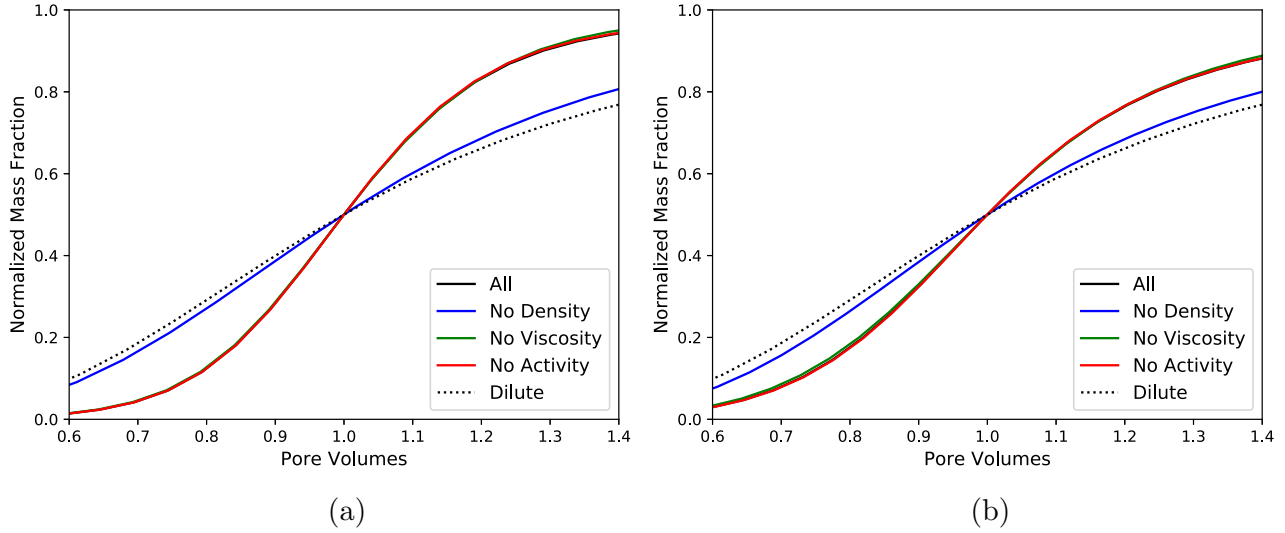
FIG. 17. Sub-REV-scale breakthrough curve sensitivity at Re $\approx 10^{-1}$: (a) $\omega_{\text{in}} = 0.4$ and $\omega_{\text{res}} = 0$; and (b) $\omega_{\text{in}} = 0.5$ and $\omega_{\text{res}} = 0.4$.

The Pe number for these simulations are large enough that diffusion is small compared to mechanical dispersion—resulting in negligible effects of viscosity on the shape of the mass fraction breakthrough curve. We conclude that at the lower Re and Pe numbers, the changes in the breakthrough curves are a result of the increased diffusion coefficient and not the neglect of viscous stabilization.

The work of Landman *et al.* [37] agree with these observations, and they concluded that viscosity impacts are only important at lower gravity numbers and larger flow rates. In their work, they found viscosity to be important at a gravity number of 0.2 but unimportant at a number of 1.64. In this work, the lowest gravity number for a nondilute displacement is 0.81. The smallest viscosity ratio ($M_{\hat{\mu}}$) for our simulations is 0.43 and according to the work of Jiao and Hötzl [62] the macroscale dispersion decreases as the viscosity ratio decreases. Our simulations agree with their work that no viscous stabilization effects may be noticed at this high of a viscosity ratio. To check this, the 1st-order parameter in the viscosity function was increased by a factor of 10 and viscous stabilization effects were observed.

3. Density

As with the viscosity, the density appears in the conservation of momentum equation and diffusion coefficient. When the density is fixed, the governing microscale equations reduce to the incompressible, constant-density form of the Navier-Stokes equations and gravity stabilization cannot occur. There is only a slight dependency of the diffusion coefficient on density (Fig. 7).

At the lower Re and Pe, the breakthrough curves are all more disperse than when density is variable (Fig. 16). As the diffusion coefficient is nearly identical with and without a variable density, these simulations are a direct measurement of gravity stabilization. As expected, the amount of gravity stabilization is a function of the incoming and resident mass fractions and more gravitational stabilization is observed as

the mass fractions increase. Since viscous stabilization is relatively unimportant at this low Re and Pe, these solutions are dominated by changes in the diffusion coefficient.

The same conclusions can be drawn from the breakthrough curves for the higher Re simulations (Fig. 17). With a constant density, we no longer have gravity stabilization and the macroscale breakthrough curves approach the dilute breakthrough curve. This shows that density impacts are the most important phenomena for macroscale nondilute transport.

D. Macroscale models

Recent attempts at modeling macroscale nondilute flow and transport have used a Taylor series expansion of Fick's law to include at least one new parameter to account for nondilute behavior [6,7]. For both of these macroscale models, the new parameters have been shown to be functions of the macroscale velocity, where the parameter decreases exponentially as the velocity increases [7,35]. From this work, we observed that as the flow rate increases for the nondilute displacements, the microscale flow field in the direction opposite to the gravity vector transitions from a distribution with negative velocities and a large variance to an exponential like distribution with a reduced variance as compared to dilute simulations. This is in agreement with the findings that dispersion decreases as the macroscale velocity increases and explains why the nondilute model parameters are functions of the macroscale velocity.

Macroscale dispersion is, however, not solely a function of the macroscale velocity and a fitting parameter. The gravity number should also be included in macroscale models because it quantifies the amount of gravity stabilization that occurs for a given macroscale velocity and includes the density differences. Egorov [32,37] developed a model that was parameter free and included the gravity number but the model was unable to correctly describe macroscale nondilute transport. The continued use of microscale simulations to increase our understanding of nondilute behavior will be necessary for the

development of high-fidelity macroscale models where the parameters are tied to the microscale physics.

VI. CONCLUSIONS

This work is the first step in obtaining a fundamental understanding of microscale nondilute flow and transport that can lead to improved and parameterized closure relations for macroscale models. From this work, we reach the following conclusions.

(1) Microscale modeling is an efficient and effective tool for advancing a fundamental understanding of complex nondilute behavior. Microscale modeling approaches are the preferred route for obtaining a mechanistic understanding as compared to macroscale laboratory experiments.

(2) Nondilute behavior can produce macroscale breakthrough curves that can be more or less disperse than dilute breakthrough curves at the same operating conditions. Additionally, an increase in the incoming salt mass fraction does not necessarily result in a sharper macroscale breakthrough curve.

(3) Density gradients are of leading order importance for nondilute flow and transport. At low Re and Pe, the chemical activity and viscosity can also affect macroscale breakthrough curves through the diffusion coefficient. At higher Re and Pe, activity impacts are unimportant and viscosity stabilization will only appear at low viscosity ratios.

(4) Gravity stabilization can result in negative microscale velocities in the mean direction of flow or a reduced variance in the mean direction of flow dependent on operating conditions.

(5) Asymmetric nondilute macroscale breakthrough curves are due to nonlinear density functions and not a result of chemical activity.

ACKNOWLEDGMENT

[1] C. T. Miller, E. H. Hill, and M. Moutier, Environ. Sci. Technol. **34**, 719 (2000).

[2] E. H. Hill, M. Moutier, J. Alfaro, and C. T. Miller, Environ. Sci. Technol. **35**, 3031 (2001).

[3] D. N. Johnson, J. A. Pedit, and C. T. Miller, Environ. Sci. Technol. **38**, 5149 (2004).

[4] W. E. Brigham, P. W. Reed, J. N. Dew *et al.*, Soc. Pet. Eng. J. **1**, 1 (1961).

[5] R. Slobod, Soc. Pet. Eng. J. **4**, 1 (1964).

[6] T. M. Weigand, P. B. Schultz, D. H. Giffen, M. W. Farthing, A. Crockett, C. T. Kelley, W. G. Gray, and C. T. Miller, Water Resour. Res. **54**, 6656 (2018).

[7] S. J. Watson, D. A. Barry, R. J. Schotting, and S. M. Hassanizadeh, Adv. Water Resour. **25**, 611 (2002).

[8] A. J. Landman, R. Schotting, A. Egorov, and D. Demidov, Adv. Water Resour. **30**, 2481 (2007).

[9] W. G. Gray and C. T. Miller, *Introduction to the Thermodynamically Constrained Averaging Theory for Porous Medium Systems* (Springer, Switzerland, 2014).

[10] J. Bear, *Dynamics of Fluids in Porous Media* (Elsevier, New York, 1972).

[11] B. Bijeljic, A. H. Muggeridge, and M. J. Blunt, Water Resour. Res. **40**, W01202 (2004).

[12] B. Bijeljic and M. J. Blunt, Water Resour. Res. **43**, W12S11 (2007).

[13] M. Icardi, G. Boccardo, D. L. Marchisio, T. Tosco, and R. Sethi, Phys. Rev. E **90**, 013032 (2014).

[14] S. Aramideh, P. P. Vlachos, and A. M. Ardekani, Phys. Rev. E **98**, 013104 (2018).

[15] B. Bijeljic, P. Mostaghimi, and M. J. Blunt, Phys. Rev. Lett. **107**, 204502 (2011).

[16] B. Bijeljic, A. Raeini, P. Mostaghimi, and M. J. Blunt, Phys. Rev. E **87** 013011 (2013).

[17] E. Crevacore, T. Tosco, R. Sethi, G. Boccardo, and D. L. Marchisio, Phys. Rev. E **94**, 053118 (2016).

[18] G. Boccardo, D. L. Marchisio, and R. Sethi, J. Colloid Interface Sci. **417**, 227 (2014).

[19] M. Siena, M. Riva, J. D. Hyman, C. L. Winter, and A. Guadagnini, Phys. Rev. E **89**, 013018 (2014).

[20] M. F. Gruber, C. J. Johnson, C. Y. Tang, M. H. Jensen, L. Yde, and C. Hélix-Nielsen, J. Membr. Sci. **379**, 488 (2011).

[21] M. F. Gruber, U. Aslak, and C. Hélix-Nielsen, Sep. Purif. Technol. **158**, 183 (2016).

[22] W. G. Gray and C. T. Miller, Adv. Water Resour. **32**, 681 (2009).

[23] W. G. Gray and C. T. Miller, Adv. Water Resour. **29**, 1745 (2006).

[24] C. T. Miller and W. G. Gray, Adv. Water Resour. **31**, 577 (2008).

[25] A. S. Jackson, C. T. Miller, and W. G. Gray, Adv. Water Resour. **32**, 779 (2009).

[26] I. V. Rybak, W. G. Gray, and C. T. Miller, J. Hydrol. **521**, 565 (2015).

[27] A. L. Dye, J. E. McClure, D. Adalsteinsson, and C. T. Miller, Water Resour. Res. **52**, 2601 (2016).

[28] J. E. McClure, A. L. Dye, C. T. Miller, and W. G. Gray, Hydrol. Earth Syst. Sci. **21**, 1063 (2017).

[29] C. T. Miller, K. Bruning, C. L. Talbot, J. E. McClure, and W. G. Gray, Water Resour. Res. **55**, 6825 (2019).

[30] K. Bruning and C. T. Miller, Water **11**, 2260 (2019).

[31] S. Hassanizadeh, Model CARE **90**, 241 (1990).

[32] A. G. Egorov, D. E. Demidov, and R. J. Schotting, Adv. Water Resour. **28**, 55 (2005).

[33] D. Demidov, Mathematical Modeling of Nonlinear Brine Transport Processes, Master's thesis, Kazan State Univeristy, 2006.

[34] R. J. Schotting, H. Moser, and S. M. Hassanizadeh, Adv. Water Resour. **22**, 665 (1999).

[35] T. M. Weigand, E. C. Harrison, and C. T. Miller, in *Proceedings of the American Geophysical Union, Fall Meeting 2017, abstract H11F-1244* (American Geophysical Union and San Francisco, CA, USA, 2017).

[36] C. Welty and L. W. Gelhar, Water Resour. Res. **27**, 2061 (1991).

[37] A. J. Landman, K. Johannsen, and R. Schotting, Adv. Water Resour. **30**, 2467 (2007).

[38] D. J. Wright, J. A. Pedit, M. W. Farthing, L. L. Murphy, G. R. Brubaker, S. R. Knight, and C. T. Miller, J. Contam. Hydrol. **115**, 46 (2009).

[39] M. Konz, A. Younes, P. Ackerer, M. Fahs, P. Huggenberger, and E. Zechner, J. Contam. Hydrol. **108**, 168 (2009).

[40] J. L. Starr and J. Y. Parlange, Soil Science **121**, 364 (1976).

[41] A. Gordon, J. Chem. Phys. **5**, 522 (1937).

[42] K. Bashar and J. H. Tellam, J. Contam. Hydrol. **122**, 40 (2011).

[43] S. Whitaker, Revista Mexicana de Ingeniería Química **8**, 213 (2009).

[44] R. B. Bird, W. E. Stewart, and E. N. Lightfoot, *Transport Phenomena*, revised 2nd ed. (John Wiley & Sons, New York, 2007).

[45] B. P. Boudreau, F. J. Meysman, and J. J. Middelburg, Earth Planet. Sci. Lett. **222**, 653 (2004).

[46] J. Bear, *Hydraulics of Groundwater* (McGraw-Hill, New York, 1979).

[47] H. G. Weller, G. Tabor, H. Jasak, and C. Fureby, Comput. Phys. **12**, 620 (1998).

[48] The open source CFD toolbox, www.openfoam.com.

[49] C. J. Greenshields, OpenFOAM User Guide, The OpenFOAM Foundation, 7th ed. (2019).

[50] J. H. Ferziger and M. Perić, *Computational Methods for Fluid Dynamics*, 3rd ed. (Springer, Berlin, 2002).

[51] R. I. Issa, J. Comput. Phys. **62**, 40 (1986).

[52] S. F. Kaslusky and K. S. Udell, J. Contam. Hydrol. **55**, 213 (2002).

[53] S. G. Johnson, The NLopt nonlinear-optimization package, http://github.com/stevengj/nlopt (2014).

[54] V. Baranau and U. Tallarek, Soft Matter **10**, 3826 (2014).

[55] S. Hauswirth, Personal Communication (2019).

[56] M. H. Schroth, S. J. Ahearn, J. S. Selker, and J. D. Istok, Soil Sci. Soc. Am. J. **60**, 1331 (1996).

[57] A. Koponen, M. Kataja, and J. Timonen, Phys. Rev. E **54**, 406 (1996).

[58] A. Duda, Z. Koza, and M. Matyka, Phys. Rev. E **84**, 036319 (2011).

[59] F. Pellegrini, Scotch and libScotch 5.1 User's Guide, user's manual (2008)

[60] D. L. Evans, J. H. Drew, and L. M. Leemis, Commun. Stat. Simul. Comput. **37**, 1396 (2008).

[61] J. S. Andrade, M. P. Almeida, J. Mendes Filho, S. Havlin, B. Suki, and H. E. Stanley, Phys. Rev. Lett. **79**, 3901 (1997).

[62] C. Y. Jiao and H. Hötzl, Transp. Porous Media **54**, 125 (2004).

[63] T. R. Noordman and J. A. Wesselingh, J. Membr. Sci. **210**, 227 (2002).

[64] L. V. D. Broeke and R. Krishna, Chem. Eng. Sci. **50**, 2507 (1995).

[65] S. M. Hassanizadeh and T. Leijnse, Water Resour. Res. **24**, 321 (1988).